Dynamic Versus Quasi-Static Analysis of Crack Propagation in Soft Materials

Suhib Abu-Qbeitah[1]
Faculty of Civil and Environmental Engineering,
Technion – Israel Institute of Technology,
Haifa 32000, Israel
e-mail: a.suhib@campus.technion.ac.il

Mahmood Jabareen
Faculty of Civil and Environmental Engineering,
Technion – Israel Institute of Technology,
Haifa 32000, Israel
e-mail: cvjmah@technion.ac.il

Konstantin Y. Volokh
Faculty of Civil and Environmental Engineering,
Technion – Israel Institute of Technology,
Haifa 32000, Israel
e-mail: cvolokh@technion.ac.il

Cracks usually propagate dynamically that makes them so dangerous. However, most crack simulations are based on quasi-static analyses because they are simpler than the dynamic ones. Is it correct to use quasi-static analyses instead of the dynamic ones? Will the quasi-static and dynamic simulations provide similar results? We try to answer these questions in the present work. We compare results of quasi-static and dynamic simulations of crack propagation in aneurysm material. We use the material-sink (MS) approach, which is based on the notion of the diffused bond breakage. The latter feature implies a local loss of material and, consequently, decrease of mass density, which, in its turn, means that both stiffness and inertia go down in the damaged zone. The cancellation of inertia is an important feature of the MS approach in contrast to more formal regularization theories as phase field, gradient damage, and other nonlocal formulations. The MS approach is implemented within commercial finite-element software ABAQUS. *A reduced mixed finite-element formulation is adopted to circumvent the volumetric locking and an implicit staggered solution algorithm is developed via the user-defined element subroutine UEL. Considered examples show that the onset of crack instability under static loads is followed by the dynamic rather than quasi-static crack propagation. Moreover, dynamic and quasi-static simulations, generally, provide different results.* [DOI: 10.1115/1.4055670]

Keywords: dynamic fracture, large deformation, soft material, material-sink method, ABAQUS

1 Introduction

A century ago, Griffith proposed a criterion for the onset of propagation of a pre-existing crack [1]. In modern terms, the criterion says that pre-existing cracks become unstable when a parameter called the energy release rate exceeds a threshold [2]. Griffith's pioneering work inspired scientists and engineers to study cracks and it initiated the research field called fracture mechanics [3,4]. Considerable theoretical [5–8] and experimental studies [9–12] were dedicated to understanding the mechanics and physics of fracture processes. The development of computers impacted fracture mechanics dramatically. Numerical simulations allowed tracking the whole process of fracture including the onset, propagation, branching, and arrest of cracks. That is far beyond the Griffith theory and analytical, often simplistic, earlier approaches to modeling fracture.

With the help of computers, fracture problems can be studied from "the first principles" on the atomic level [13]. For example, methods of molecular dynamics are sometimes utilized [14,15]. However, considerations of the atomic length and time scales are computationally demanding and, because of that, they are hardly practical for engineering applications. More practical would be the so-called discrete models within the framework of continuum mechanics. In such models, cracks are presented by the placement discontinuities along surfaces of zero thickness [16–28]. Among discrete approaches, we mention cohesive surface models (CSM), which define the placement discontinuities by traction-separation laws. The insertion of cohesive surfaces is especially effective along the weak material interfaces known in advance. In the cases where the weak interface is not known in advance, the CSM might not be the best option. A possible alternative might be the eXtended finite-element approach (XFEM) [23,29]. Remarkably, the XFEM does not need re-meshing. Unfortunately, XFEM requires additional efforts to model crack branching and complex spatial crack patterns [30,31].

In contrast to the mentioned discrete approaches, continuous methods [32–39] characterize cracks as damaged regions of small yet finite thickness. The bulk material obeys constitutive laws in which the stress falls after a maximum critical limit indicating material damage and its localization into crack. Such constitutive description leads to an easy modeling of the crack onset, propagation, branching, and arrest. Thus, the whole fracture process comes out naturally as a solution of an initial boundary value problem. However, this continuum damage approach is not short of disadvantages as well. The main one is the so-called pathological mesh-dependence: the finer the mesh, the smaller the dissipated fracture energy. Ultimately, a crack might dissipate zero energy for a vanishing mesh size. That is unacceptable. Various theories have been formulated to circumvent the pathological mesh-dependence. For example, nonlocal continuum formulations [40–44] have been developed and their extensive applications to engineering problems have been reported in the literature.

Recently, phase field methods (PFMs) [45–57] gained popularity for modeling cracks. In PFMs, cracks are presented by a dimensionless scalar variable – phase field. This variable equals one for the crack and zero for the intact material. It varies smoothly between these two extremes. The phase field variable is described implicitly by a special partial differential equation (PDE) involving characteristic length at the highest spatial derivatives. Such feature provides solutions of the boundary-layer type and suppresses the pathological mesh-sensitivity. The latter property makes the PFM very favorable in modeling complex fracture including crack branching. However, the physical meaning of the phase field variable and its governing equation are vague. The formal nature of PFMs manifests itself in statements that the solutions of the boundary value problems should converge to the ideal zero thickness Griffith's crack under decrease of the characteristic length. Such statements are incorrect because the characteristic length is a physical rather than a numerical parameter and its variation leads to different physical models and processes.

[1]Corresponding author.

Contributed by the Applied Mechanics Division of ASME for publication in the JOURNAL OF APPLIED MECHANICS. Manuscript received September 8, 2022; final manuscript received September 13, 2022; published online October 6, 2022. Tech. Editor: Pradeep Sharma.

In this work, we adopt the material-sink (MS) formulation proposed by Volokh [58] as an extension to the energy limiter approach [59–64]. In particular, the MS theory is used to study dynamic versus quasi-static crack propagation in an aneurysm material. In all considered examples, the load is applied very slowly—quasi-statically—while the subsequent crack propagation is tracked dynamically. Results of the dynamic analyses are compared to the quasi-static ones from Abu-Qbeitah et al. [65]. The results show that cracks propagate dynamically and, consequently, they should be analyzed dynamically. Quasi-static analyses tend to "stabilize" the fracture process, which is unstable in reality.

The subsequent sections are organized as follows: Sec. 2 summarizes the material-sink theory presenting the underlying balance and constitutive equations. The finite-element formulation is briefly described in Sec. 3. Section 4 explains the algorithm implementation in ABAQUS. Numerical examples are presented in Sec. 5 and conclusions are drawn in Sec. 6.

2 Material-Sink Theory

The material-sink theory was proposed in Ref. [58] based on the physical notion of the diffused bond breakage. This notion is not trivial because we are used to tacitly assume that crack is a result of unzipping of two adjacent atomic layers. Such an assumption is appealing due to its simplicity. However, new material surfaces, characterizing crack, can appear as a result of the massive bond breakage spread over a region with characteristic size l (Fig. 1). The very fact that we can see closed cracks with the naked eye supports the assumption of the diffused damage.

The massive bond breakage leads to the local loss of material, atoms, and molecules. Thus, mass is not conserved locally in the cracked region. The latter notion means that the mass density is a variable that changes from its initial value to zero for crack. In other words, the mass density is a damage variable. Furthermore, since the mass density is a variable that diminishes in the fractured region then material loses stiffness along with *inertia*!

Remarkably, the mass loss during fracture process in concrete is visible because it is often accompanied by disintegration of small pieces and concrete dust. The mass loss in soft materials is hardly visible yet the molecular debris can be smelled, sometimes.

Mathematical formulation of the MS theory includes coupled mass and momentum balance laws within the framework of continuum mechanics. We consider a generic material point $\mathbf{X}$ in the initial configuration $\mathcal{B}_0$ with boundary $\partial\mathcal{B}_0$. The point moves to position $\mathbf{x}$ in the current configuration $\mathcal{B}$ with boundary $\partial\mathcal{B}$. We define the deformation gradient $\mathbf{F}=\operatorname{Grad}\mathbf{x}$ with respect to $\mathbf{X}$. Henceforth, we use the Lagrangian description.

Following Ref. [58], we set the mass balance in the form

$$\operatorname{Div}\mathbf{s}+\xi=0 \tag{1}$$

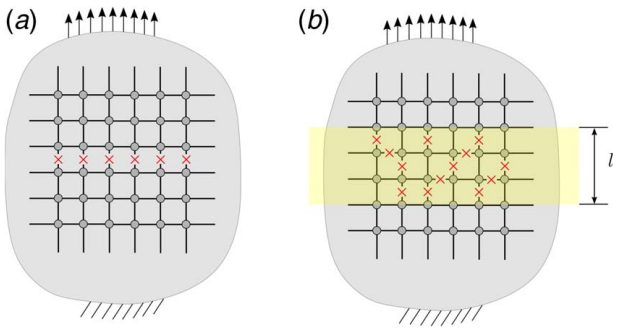

Fig. 1 Schematic drawing of a crack with zero or finite thickness: (*a*) unzipping of two adjacent atomic or molecular layers and (*b*) development of multiple micro-cracks triggered by the massive breakage of molecular or atomic bonds

where $\mathbf{s}$ and ξ are the referential mass flux and source (sink) accordingly and the divergence operator is defined with respect to $\mathbf{X}$.

The momenta balance are set in the form

$$\rho\mathbf{a}=\operatorname{Div}(\mathbf{FS}),\quad \mathbf{S}=\mathbf{S}^{\mathrm{T}} \tag{2}$$

where ρ is the referential mass density; $\mathbf{S}$ is the second Piola–Kirchhoff (PK) stress tensor; and $\mathbf{a}$ is the acceleration vector.

The natural boundary conditions express the mass and momentum balance on $\partial\mathcal{B}_0$ as follows:

$$\begin{aligned}&\mathbf{s}\cdot\mathbf{N}=0\\&\mathbf{FSN}=\bar{\mathbf{t}}_0\end{aligned} \tag{3}$$

where $\mathbf{N}$ is the unit outward normal to $\partial\mathcal{B}_0$ and $\bar{\mathbf{t}}_0$ denotes the prescribed traction.

The second Piola–Kirchhoff stress $\mathbf{S}$ is defined by constitutive equation

$$\mathbf{S}=2\rho\frac{\partial w}{\partial\mathbf{C}} \tag{4}$$

in which w denotes the specific (per unit mass) Helmholtz free energy, and $\mathbf{C}$ denotes the right Cauchy–Green tensor $\mathbf{C}=\mathbf{F}^{\mathrm{T}}\mathbf{F}$.

Constitutive laws for the mass flux and sink are defined as follows respectively [58,65]

$$\begin{aligned}&\mathbf{s}=\kappa\operatorname{Grad}\rho\\&\xi=\beta\rho_0-\beta\rho\mathrm{e}^{(w/\phi)^m}\end{aligned} \tag{5}$$

where $\rho_0=\rho(t=0)$ is the initial mass density and β, κ, m, and ϕ are positive material parameters.

Substituting Eq. (5) into Eq. (1) yields

$$\operatorname{Div}\mathbf{f}+\zeta=0 \tag{6}$$

where

$$\begin{aligned}&\mathbf{f}=l^2\operatorname{Grad}\gamma\\&\zeta=1-\gamma\mathrm{e}^{(W/\Phi)^m}\end{aligned} \tag{7}$$

and

$$\gamma=\rho/\rho_0,\quad l=\sqrt{\frac{\kappa}{\beta}},\quad W=\rho_0 w,\quad \Phi=\rho_0\phi \tag{8}$$

The introduced characteristic length l controls the width of the damaged region and parameters β and κ are not needed separately. Furthermore, γ, W, and Φ are the relative mass density, the Helmholtz free energy, and the energy limiter per unit reference volume, accordingly.

In numerical simulations, we enforce the irreversibility of the damage by modifying the mass sink law as follows:

$$\zeta=1-\frac{\gamma}{\mathcal{H}+\varepsilon} \tag{9}$$

where $\varepsilon=10^{-15}$ is a small number for numerical stabilization and the exponential term is replaced by the history-field variable $\mathcal{H}$ defined as

$$\mathcal{H}(t_0)=1,\quad \mathcal{H}(t_{n+1})=\min\left\{\begin{matrix}\mathrm{e}^{-(W/\Phi)^m}\\ \mathcal{H}(t_n)\end{matrix}\right\} \tag{10}$$

We can rewrite the constitutive law for stresses in terms of the new variables as follows:

$$\mathbf{S}=\gamma\mathbf{S}_0,\quad \mathbf{S}_0=2\frac{\partial W}{\partial\mathbf{C}} \tag{11}$$

where $\mathbf{S}_0$ can be interpreted as the "undamaged" second Piola–Kirchhoff stress.

3 Numerical Formulation

There is always the question of whether the monolithic or the staggered approach should be used to model coupled problems. In the particular case of modeling unstable crack propagation, the monolithic solution becomes numerically unstable [2]. However, there are various techniques that can be used to improve the monolithic solution [66–68]. Nonetheless, none of them is suitable for the code implemented in ABAQUS [2].

The present work uses the staggered scheme, where the proposed technique provides outstanding robustness to the solver. It is based on the idea that the displacement and relative mass density fields are coupled only weakly. In each iteration, both fields are independent and solved at the same time independently based on the variables calculated from the previous iteration as depicted in Fig. 2.

3.1 A Reduced Mixed Finite-Element Formulation. A reduced mixed finite-element method proposed by Bishara and Jabareen [69] and Jabareen [70] is adopted to model the aneurysm material, since the standard finite-element method suffers from volumetric locking when used to model nearly and fully incompressible materials.

Following Refs. [69,70], the deformation tensor is decomposed into volumetric and distortional components. The point-to-point volumetric measure is replaced by an averaged one, while the point-to-point distortional measure stays as it is. Thus, the modified deformation tensor can be expressed as

$$\overline{\mathbf{C}} = \underbrace{\overline{J}^{2/3}\mathbf{I}}_{\overline{\mathbf{C}}_{\text{vol.}}} \underbrace{J^{-2/3}\mathbf{C}}_{\overline{\mathbf{C}}_{\text{dis.}}} = \left(\frac{\overline{J}}{J}\right)^{2/3}\mathbf{C} \tag{12}$$

where $\overline{J}$ is a scalar related to the volumetric dilatation that can be expressed as

$$\overline{J} = \frac{1}{\Omega_0^{\text{e}}}\int_{\Omega_0^{\text{e}}} J\,\mathrm{d}\Omega_0^{\text{e}} \tag{13}$$

where Ω_0^{e} is the element referential volume. In the following subsections, the general procedure of the reduced mixed finite-element method is discussed. For more details, interested readers are advised to consult [65].

3.1.1 Discretization of the Momentum Balance Law. The weak form of the momentum equation $\delta\Pi_{MO}$ is given by $\delta\Pi_{MO} = \sum_{e=1}^{N_{el}} \delta\Pi_{MO}^{e} = -\delta\Pi_{\text{kin}}$, in which $\delta\Pi_{MO}^{e}$ is expressed as

$$\delta\Pi_{MO}^{\text{e}} = \int_{\Omega_0^{\text{e}}} \left(\overline{\mathbf{S}} : \delta\overline{\mathbf{E}}\right)\mathrm{d}\Omega_0^{\text{e}} - \int_{\partial\mathcal{B}_0^{t_0}} \bar{\mathbf{t}} \cdot \delta\mathbf{u}\,\mathrm{d}\Gamma_0 \tag{14}$$

where Π_{kin} is the kinetic energy, $\{\overline{\mathbf{S}}, \overline{\mathbf{E}}\}$ are the modified second Piola–Kirchhoff stress and the modified Green–Lagrange strain tensor, respectively. Modified quantities are evaluated using the modified right Cauchy–Green deformation tensor (Eq. (12)) and the average volumetric deformation (Eq. (13)). Since now on, any quantity with an over-line means that the quantity is modified.

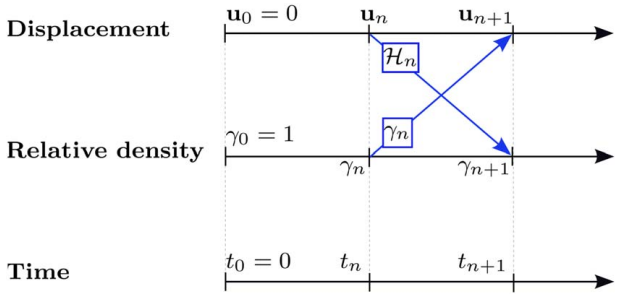

Fig. 2 Flowchart of the staggered scheme that is employed to solve the coupled displacement–relative density system in ABAQUS

To derive the tangent stiffness of the momentum problem, a linearization of Eq. (14) is needed that is expressed as

$$\Delta\delta\Pi_{MO}^{\text{e}} = \int_{\Omega_0^{\text{e}}} \left(\delta\overline{\mathbf{E}} : \overline{\mathbb{C}}_{uu} : \Delta\overline{\mathbf{E}} + \overline{\mathbf{S}} : \Delta\delta\overline{\mathbf{E}}\right) d\Omega_0^{\text{e}} \tag{15}$$

where the modulus $\overline{\mathbb{C}}_{uu}$ is determined by

$$\overline{\mathbb{C}}_{uu} = \gamma\overline{\mathbb{C}}_{uu0}, \quad \overline{\mathbb{C}}_{uu0} = 4\left.\frac{\partial^2 W}{\partial\mathbf{C}\partial\mathbf{C}}\right|_{\left\{J=\overline{J},\,\mathbf{C}=\overline{\mathbf{C}}\right\}} \tag{16}$$

Additionally, it is more advantageous to employ the Voigt shorthand notation. Precisely, in the Voigt notation, first- and second-order tensors are represented as vectors indicated by a single underline. Likewise, fourth-order tensors are represented by matrices indicated by a double underline.

Accordingly, the internal and external forces are given by

$$\widehat{\underline{\mathbf{F}}}_{u}^{\text{int,e}} = \int_{\Omega_0^{\text{e}}} \underline{\overline{\mathbf{B}}}_{u}^{\text{T}}\underline{\overline{\mathbf{S}}}\,\mathrm{d}\Omega_0^{\text{e}}, \quad \widehat{\underline{\mathbf{F}}}_{u}^{\text{ext,e}} = \int_{\partial\mathcal{B}_0^{t_0}} \underline{\overline{\mathbf{N}}}_{u}^{\text{T}}\underline{\bar{\mathbf{t}}}\,d\Gamma_0 \tag{17}$$

where $\overline{\mathbf{S}}$ denotes a vector of the entries of the second PK stress tensor. The matrix $\underline{\overline{\mathbf{B}}}_{u}$ contains the components of the deformation gradient and the derivatives of the shape functions, while the matrix $\underline{\overline{\mathbf{N}}}_{u}$ contains the shape functions. For more details about the latter quantities, interested readers are referred to Ref. [65].

The displacement tangent stiffness matrix has the following form:

$$\underline{\underline{\mathbf{K}}}_{uu}^{\text{e}} = \int_{\Omega_0^{\text{e}}} \left(\underline{\overline{\mathbf{B}}}_{u}^{\text{T}}\underline{\underline{\overline{\mathbf{D}}}}_{uu}\underline{\overline{\mathbf{B}}}_{u} + \underline{\underline{\overline{\mathbf{k}}}}_{G}^{\text{e}}\right) d\Omega_0^{\text{e}} \tag{18}$$

where $\underline{\underline{\overline{\mathbf{D}}}}_{uu}$ is the matrix form of the tensor $\overline{\mathbb{C}}_{uu}$, and $\underline{\underline{\overline{\mathbf{k}}}}_{G}^{\text{e}}$ is the geometrical tangent stiffness matrix per unit referential volume, which is given by

$$\underline{\underline{\overline{\mathbf{k}}}}_{G}^{\text{e}} = \sum_{i=1}^{3}\sum_{j=1}^{3} \overline{S}_{ij}\frac{\partial^2\Delta\delta\overline{E}_{ij}}{\partial\delta\underline{\widehat{\mathbf{u}}}\partial\Delta\underline{\widehat{\mathbf{u}}}} \tag{19}$$

For more information about the derivation of $\underline{\underline{\overline{\mathbf{k}}}}_{G}^{\text{e}}$, interested readers are referred to Ref. [65].

3.1.2 Discretization of the Mass Balance Law. The weak form of the mass balance equation $\delta\Pi_{MA}$ is given by $\delta\Pi_{MA} = \sum_{e=1}^{N_{el}} \delta\Pi_{MA}^{e} = 0$, in which $\delta\Pi_{MA}^{e}$ is expressed as

$$\delta\Pi_{MA}^{\text{e}} = \int_{\Omega_0^{\text{e}}} \left(-\mathbf{f}\cdot\mathrm{Grad}\left(\delta\gamma\right) + \overline{\zeta}\delta\gamma\right) d\Omega_0^{\text{e}} \tag{20}$$

For deriving the stiffness matrix of the mass balance problem, a linearization of Eq. (20) is needed, which is expressed as

$$\Delta\delta\Pi_{MA}^{\text{e}} = -\int_{\Omega_0^{\text{e}}} \mathrm{Grad}(\delta\gamma)\cdot\mathbf{C}_{\gamma\gamma}\cdot\mathrm{Grad}\left(\Delta\gamma\right) d\Omega_0^{\text{e}} + \int_{\Omega_0^{\text{e}}} \delta\gamma\overline{\mathrm{C}}_{\gamma\gamma}\Delta\gamma\,\mathrm{d}\Omega_0^{\text{e}} \tag{21}$$

where the second-order tensor $\mathbf{C}_{\gamma\gamma}$ and the scalar $\overline{\mathrm{C}}_{\gamma\gamma}$ are expressed as

$$\begin{aligned} \mathbf{C}_{\gamma\gamma} &= \frac{\partial\mathbf{f}}{\partial\left(\mathrm{Grad}\left(\gamma\right)\right)} = l^2\mathbf{I} \\ \overline{\mathrm{C}}_{\gamma\gamma} &= \left.\frac{\partial\overline{\zeta}}{\partial\gamma}\right|_{\left\{J=\overline{J},\,\mathbf{C}=\overline{\mathbf{C}}\right\}} = -\frac{1}{\overline{\mathcal{H}}+\varepsilon} \end{aligned} \tag{22}$$

where the history-field $\overline{\mathcal{H}}$ is determined by Eq. (10), where $\{\overline{J}, \overline{\mathbf{C}}\}$ are used instead of $\{J, \mathbf{C}\}$.

The internal force is articulated as

$$\underline{\widehat{\mathbf{F}}}_{\gamma}^{\mathrm{int,e}} = \int_{\Omega_0^{\mathrm{e}}} \left(-\underline{\underline{\mathbf{B}}}_{\gamma}^{\mathrm{T}} \underline{\mathbf{f}} + \underline{\mathbf{N}}_{\gamma}^{\mathrm{T}} \bar{\zeta} \right) \mathrm{d}\Omega_0^{\mathrm{e}} \tag{23}$$

where the matrix $\underline{\underline{\mathbf{B}}}_{\gamma}$ contains the derivatives of the shape functions. The row vector $\underline{\mathbf{N}}_{\gamma}$ contains the shape functions. For more information about their values, interested readers are referred to Ref. [65].

The tangent stiffness matrix of the relative density field $\underline{\underline{\mathbf{K}}}_{\gamma\gamma}^{\mathrm{e}}$ has the following form:

$$\underline{\underline{\mathbf{K}}}_{\gamma\gamma}^{\mathrm{e}} = \int_{\Omega_0^{\mathrm{e}}} \left(-\underline{\underline{\mathbf{B}}}_{\gamma}^{\mathrm{T}} \underline{\underline{\mathbf{D}}}_{\gamma\gamma} \underline{\underline{\mathbf{B}}}_{\gamma} + \underline{\mathbf{N}}_{\gamma}^{\mathrm{T}} \overline{\mathrm{C}}_{\gamma\gamma} \underline{\mathbf{N}}_{\gamma} \right) \mathrm{d}\Omega_0^{\mathrm{e}} \tag{24}$$

where $\underline{\underline{\mathbf{D}}}_{\gamma\gamma}$ is the matrix form of the tensor $\mathbf{C}_{\gamma\gamma}$.

3.2 Time Integration. For dynamic cases, ABAQUS uses the Hilber–Hughes–Taylor (HHT) time integration [71]. The HHT operator is an extension of the Newmark β-method [72]. This time integration operator is implicit. This means that a set of nonlinear differential equations are iteratively solved at each time-step by Newton's method.

The main advantage of this implicit operator is that it is unconditionally stable. In other words, there is no mathematical limit on the time-step size. Such an operator is of great importance when studying crack propagation because a conditionally stable operator (e.g., the one used in the explicit method) may lead to unpractical small time-steps leading to large simulation time [72].

HHT solves the linearized equilibrium equations by applying the following Newton–Raphson iteration:

$$\begin{bmatrix} \underline{\underline{\mathbf{S}}}_n^{\mathrm{u}} & \mathbf{0} \\ \mathbf{0} & (1+\alpha)\underline{\mathbf{K}}_n^{\gamma} \end{bmatrix} \begin{Bmatrix} \Delta\widehat{\underline{\mathbf{u}}}_n \\ \Delta\widehat{\gamma}_n \end{Bmatrix} = -\begin{bmatrix} \widehat{\underline{\mathbf{r}}}_n^{u} \\ \alpha\widehat{\underline{\mathbf{r}}}_{n-1}^{\gamma} - (1+\alpha)\widehat{\underline{\mathbf{r}}}_n^{\gamma} \end{bmatrix} \tag{25}$$

In the dynamic case, the displacement residual $\widehat{\underline{\mathbf{r}}}_n^{u}$ contains an inertial part as well, which can be written as

$$\widehat{\underline{\mathbf{r}}}_n^{u} = (1+\alpha)\widehat{\underline{\mathbf{F}}}_n^{\mathrm{int,u}} - \alpha\widehat{\underline{\mathbf{F}}}_{n-1}^{\mathrm{int,u}} + \widehat{\underline{\mathbf{F}}}_n^{\mathrm{inertia}} - \widehat{\underline{\mathbf{F}}}_n^{\mathrm{ext,u}} \tag{26}$$

where $\widehat{\underline{\mathbf{F}}}_n^{\mathrm{ext,u}}$ is the external and $\widehat{\underline{\mathbf{F}}}_n^{\mathrm{int,u}}$ is the internal force vectors. Parameter α is a damping coefficient. The stiffness matrix of the displacement problem contains both tangent stiffness $\underline{\underline{\mathbf{K}}}_n^{\mathrm{u}}$ and mass $\underline{\underline{\mathbf{M}}}$ matrices

$$\underline{\underline{\mathbf{S}}}_n^{\mathrm{u}} = \underline{\underline{\mathbf{M}}} \frac{\mathrm{d}\dot{u}}{\mathrm{d}u} + (1+\alpha)\underline{\underline{\mathbf{K}}}_n^{\mathrm{u}} \tag{27}$$

in which the mass matrix $\underline{\underline{\mathbf{M}}}$ can be expressed as

$$\underline{\underline{\mathbf{M}}} = \int_{\Omega_0^{\mathrm{e}}} \gamma\rho_0 \underline{\underline{\mathbf{N}}}_u^{\mathrm{T}} \underline{\underline{\mathbf{N}}}_u \, \mathrm{d}\Omega_0^{\mathrm{e}} \tag{28}$$

and the acceleration derivative takes the following form with $\beta = (1-\alpha)^2/4$:

$$\frac{\mathrm{d}\dot{u}}{\mathrm{d}u} = \frac{1}{\beta\Delta t^2} \tag{29}$$

It can be noticed from Eq. (28) that the mass is not conserved within the fractured zone.

4 ABAQUS Implementation

The user-defined element subroutine *UEL* is used to implement the MS method. In the *UEL*, the user should code the subroutine to calculate the element's residual vector *RHS*, as well as the element's matrix *AMATRX* based on the nodal degrees of freedom values passed by ABAQUS.

The coupled system of fracture and large deformation is implemented via the staggered scheme, where the sharp crack is regularized by the relative density which is calculated based on the history field. Then, the relative density field is used to recalculate the displacement distribution as depicted in Fig. 2.

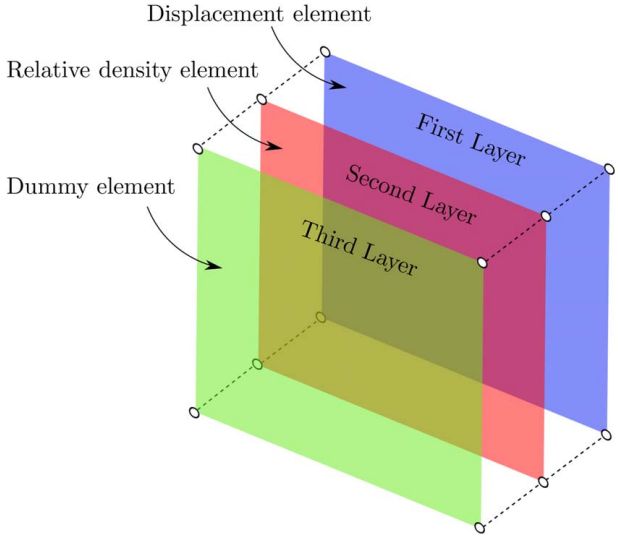

Fig. 3 Schematic representation of the three-layered finite-element structure in ABAQUS. The first element contributes to the stiffness of the displacement DOFs made as a UEL model; the second element contributes to the relative density (damage) DOF made as a UEL model. For post-processing purposes, a third layer is included made as a UMAT model, which allows displaying state-dependent variables (SDVs).

Three layers of elements are used. The first two layers are used to solve the coupled problem and the third layer is used for visualization purposes. All layers share the same nodes. However, each layer of the first two layers contributes to a different degree of freedom. A schematic illustration is depicted in Fig. 3. The first layer solves the momentum problem, so it has displacement DOFs (1, 2 for the two-dimensional case or 1, 2, 3 for the three-dimensional case). Whereas, the second layer solves the mass balance problem so it has a density DOF (11).[2]

One drawback of using the *UEL* subroutine is that the results cannot be visualized by the standard tool ABAQUS/VIEWER. The latter is due to the fact that the element topology is hidden inside the subroutine [73]. Thus, in order to visualize the results, a third layer is created from UMAT subroutine, which overlays the first two layers. Furthermore, it is used to transfer information from the *common* block. It is important to note that this element should have the same number of nodes and the same number of Gauss points as the user elements. Furthermore, this layer should have negligible stiffness to make sure its presence will not affect the main problem.

Failed elements[3] may cause convergence issues due to their excessive distortion. Thus, they should be deleted from the mesh. Since three layers of elements are used, the three layers should be deleted at the same time once the deletion criterion is satisfied. The latter means deleting the user elements and the dummy element simultaneously. For deleting the dummy element, ABAQUS provides the possibility to delete it using the state-dependent variables (SDVs) controlled by the user subroutine UMAT. On the other hand, for deleting the user elements, the internal forces should be set to zero and the stiffness matrices to a very small value. Specifically, the stiffness matrices were set to 10^{-6} from their calculated values.

[2]The temperature degree of freedom (i.e., 11) is used to store the relative density DOF.

[3]An element is defined as a failed element if the relative density values at all integration points are less than or equal to 10^{-6}.

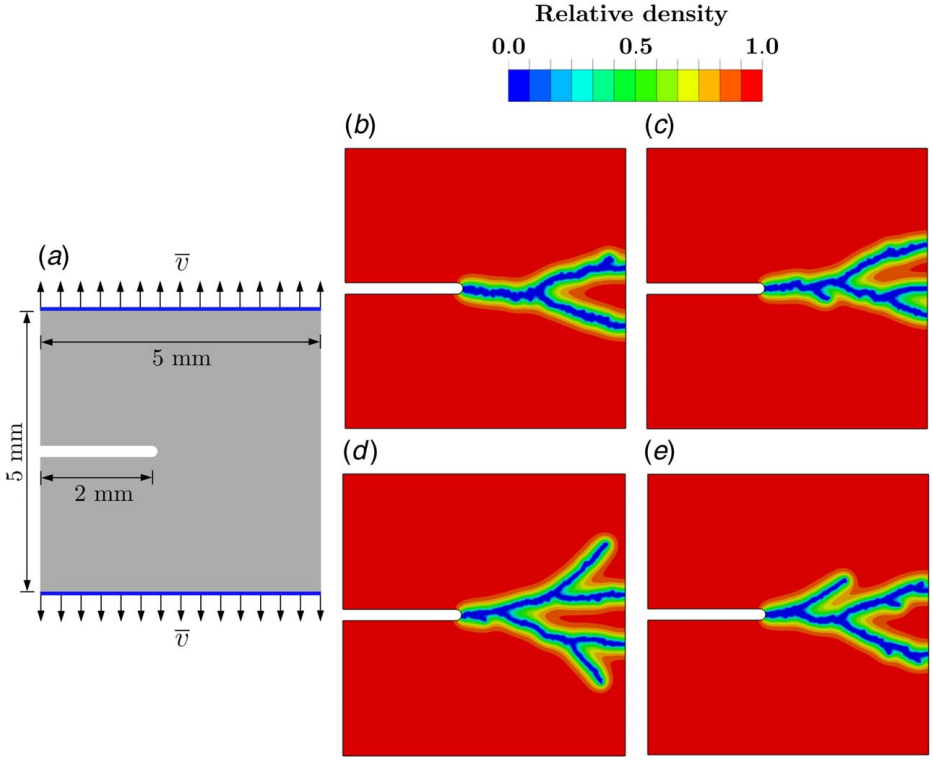

Fig. 4 Single-edge notched tensile sample: (*a*) geometry and boundary conditions; relative density (i.e., γ) distribution when the applied velocity $\overline{v}$ equals 10^{-3} mm/s for different meshes (*b*) M3, (c) M4, (*d*) M5; and (e) relative density contours when the applied velocity $\overline{v}$ equals 10^{-15} mm/s for the M4 mesh

Following Refs. [59–64], the energy—per unit depth—dissipated during fracture determined for each failed element can be expressed as

$$U_i = A_i \psi_{\mathrm{f}} = A_i \Phi m^{-1} \Gamma[m^{-1},\ W(\mathbf{I})^m \Phi^{-m}] \tag{30}$$

where A_i is the referential area of the ith failed element.

5 Numerical Examples

To test whether cracks propagate dynamically or quasi-statically, 2D and 3D well-known examples are analyzed dynamically under a slowly applying load. The latter results are compared to the results from quasi-static analysis conducted by Abu-Qbeitah et al. [65]. The 2D examples[4] are discretized with quadrilateral elements, while the 3D examples are discretized with eight-node blocks.

In particular, the strain energy function used in this study can be defined as follows:

$$W = \frac{1}{2} k_{\mathrm{bulk}} (J-1)^2 + c_1 \left(I_1' - 3\right) + c_2 \left(I_1' - 3\right)^2 \tag{31}$$

where I_1' is the first invariant of the distortional component of $\mathbf{C}$ (i.e. $J^{-2/3}\mathbf{C}$), k_{bulk} is the bulk modulus, and $\{c_1,\ c_2\}$ are material parameters.

The material under consideration is a sample from an abdominal aortic aneurysm (AAA),[5] which was fitted by Faye et al. [74] to the experimental data carried out by Raghavan et al. [75]. The material parameters are $c_1 = 0.617$ MPa, $c_2 = 1.215$ MPa, $k_{\mathrm{bulk}} = 500$ MPa, $\Phi = 0.1686$ MPa, $m = 10$, $l = 0.1$ mm, and $\rho_0 = 1433$ kg/m^3. The parameters for the HHT integrator, $\alpha = -0.05$ and $\beta = 0.275625$, are adopted. Substituting for Φ and m in Eq. (30) yields the dissipated energy per unit depth for each failed element that is expressed as

$$U_i = 0.95 A_i \Phi \tag{32}$$

It is worth mentioning that unstructured meshes are adopted in all examples modeled in this study.

5.1 Single-Edge Notched Tensile Sample.

This example tests the theory in modeling mode I fracture, where a square plate with an edged pre-existing notch under an applied uniaxial tension is modeled as shown in Fig. 4(*a*).

Three unstructured meshes are used as tabulated in Table 1. The ID of each mesh is tabulated in the first column, where in this notation the number after the letter M characterizes the ratio of the characteristic length to the element's size. Thus, for M3, M4, and M5 the characteristic length is 3, 4, and 5 times the element mesh size, respectively. It is noteworthy that in all meshes the characteristic length is fixed and only the element's size is changed with respect to the characteristic length. The latter note is important since the characteristic length is a material parameter and cannot be changed freely.

Table 1 Meshes' details with corresponding dissipated energies for the single-edge notched tensile sample

ID	Element size	Number of elements	Dissipated energy (N mm/mm)
M3	$l/3$	11,140	0.067
M4	$l/4$	18,967	0.064
M5	$l/5$	28,784	0.068

[4]Plain strain condition is assumed in all 2D examples.

[5]An AAA is an enlarged area in the lower part of the aorta, which is the largest blood vessel in the body, running from the heart through the center of the chest and abdomen.

The sample's top and bottom ends are under an applied small velocity that has a value of 0.001 mm/s in the vertical direction. Figures 4(*b*)–(*d*) show the relative density contours in M3, M4, and M5 meshes, respectively. A value of 1 means that the material is fully intact, whereas a value of 0 means that the material is fully fractured. Thus, in the regularized zone, the relative density γ has a spectrum of values ranging between 0 and 1.

It can be noticed from Fig. 4 that the crack propagates dynamically in all meshes although the load is applied slowly. On the other hand, the crack propagation path in the quasi-static paper [65] as shown in Fig. 11(*a*), for the same example, was a straight line that initiated from the pre-existing notch and reached the end of the sample. However, the result from the dynamic modeling in Fig. 4 shows that the crack branches and propagates dynamically even if the load is applied quasi-statically.

The dissipated energies for each mesh are calculated using Eq. (32) and summarized in Table 1. The dissipated energy values are almost the same in all meshes. It can be noticed from Fig. 4 that in the finer meshes the crack thickness is smaller. Thus, to maintain the same dissipated energy, the crack propagating in the finer mesh tends to branch more.

Figure 4(*e*) shows the relative density contours for the case when the applied velocity is smaller ($\overline{v} = 10^{-15}$ mm/s). The result suggests that it does not matter how much the applied velocity is small, the crack always propagates dynamically. It is noteworthy to notice the obvious crack arrest phenomenon in Fig. 4(*e*). The crack in its first branching branched into two, where one of those two branches stopped, while the other branch continued propagating that branched further.

It can be concluded from this example that crack propagation is a dynamic process, where the quasi-static analysis is not able to capture the real behavior of the material. The latter conclusion is justified by the fact that the crack patterns from both quasi-static and dynamic analyses are different.

5.2 Simple Shear Test. A simple shear test is considered in this subsection to test the theory in mode II fracture. It is used as a benchmark example in the literature, where the specimen in this test is under a combination of tension and compression loads within the sample during shear [76]. The sample has a pre-existing notch at its left edge. In Fig. 5(*a*), the geometry of the model is depicted. The top edge is under a velocity of 10^{-3} mm/s applied in the *x*-direction, while the bottom edge is fixed in both the horizontal and vertical directions. The sample is discretized by 50,847 quadrilateral elements of an unstructured mesh.

Figures 5(*b*) and (*c*) show the relative density contours under different levels of remote shear, where no branching is noticed. On the other hand, the result from the quasi-static analysis is shown in Fig. 11(*b*). Although the crack pattern for the dynamic and quasi-static analyses is similar, the dissipated energies are different. We notice that by comparing the width of each crack, where the width of the dynamic crack is larger. The dissipated energies are calculated using Eq. (32) and equal 0.036 N mm/mm and 0.023 N mm/mm for the dynamic and quasi-static analyses, respectively. On the other hand, the results show that the tendency for branching is much less in mode II compared to mode I. The latter note implies that the crack's path should not always have branching to be proclaimed as a dynamic propagation. That is to say, in this example, the crack has less tendency to branch since it is a mode II fracture. However, the crack propagation is still dynamic, propagating at high velocity and dissipating more energy compared to the quasi-static analysis.

The results show that the crack initiates from the pre-existing notch and propagates exclusively into the tensile part. The crack propagates in the tensile region without the need to differentiate between the tensile and the compressive parts of the strain energy. Such a need can be suppressed because the material's tensile and compressive strengths are asymmetric in the case of large deformation.

5.3 Symmetric Double-Edge Notched Tensile Sample. A sample with two symmetric notches is analyzed in this subsection. The geometry and boundary conditions are depicted in Fig. 6(*a*). A small velocity boundary condition is applied at the top and bottom surfaces in the vertical direction having a value of 10^{-3} mm/s.

Figures 6(*b*) and (*c*) show the relative density contours at different levels of remote tension. Two cracks propagate from both notches with high velocity in straight lines, then each crack branches into two, where the branch that is close to the crack, coming from the other side, continues propagating, while the remaining branch arrests. Finally, both cracks merge and the sample is completely fractured into two pieces.

Figure 11(*c*) shows the relative density contours, for the same example, from the quasi-static analysis. Two cracks propagated from both sides of the pre-existing notches in straight lines that finally merged. By comparing the results from the dynamic analysis (Fig. 6(*c*)) versus the quasi-static analysis (Fig. 11(*c*)), it is clear that the crack patterns are different. Although there is a similarity between the two crack patterns, the dynamic analysis captures branching and arrest phenomena that had not been captured using the quasi-static analysis.

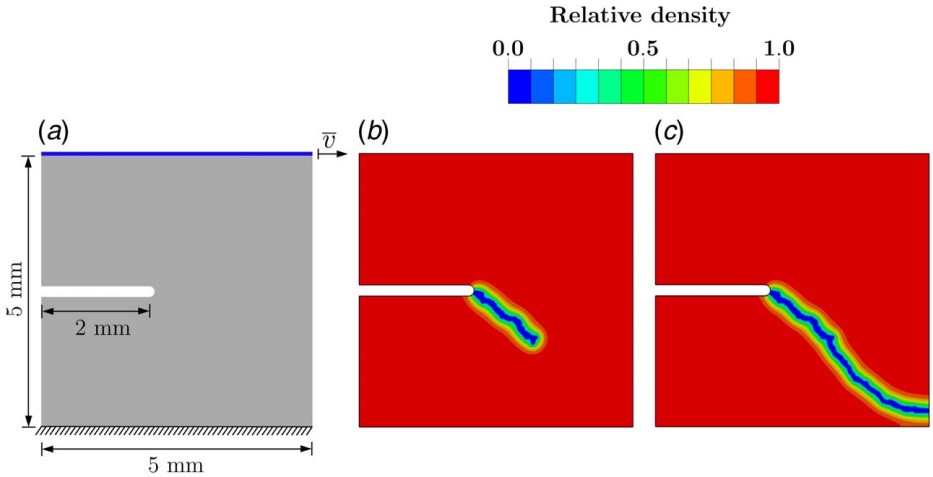

Fig. 5 Simple shear test: (*a*) geometry and boundary conditions, and (*b*) and (c) relative density (i.e., γ) distribution under different levels of remote shear

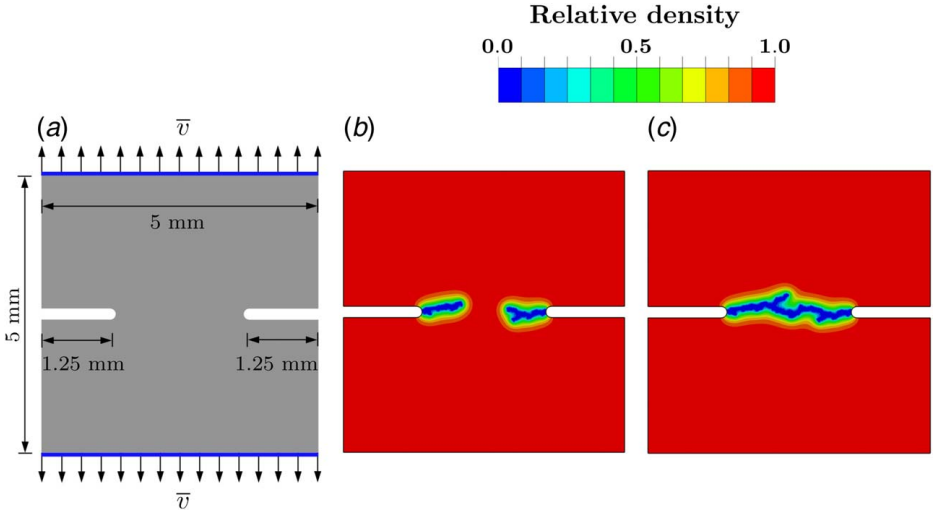

Fig. 6 Symmetric double-edge notched tensile sample: (*a*) geometry and boundary conditions with an applied velocity $\overline{v}$ equals 10^{-3} mm/s and (*b*) and (c) relative density (i.e., γ) distribution under different levels of remote tension

Furthermore, the energy dissipated from both analyses is calculated using Eq. (32) to be 0.0295 N mm/mm and 0.0140 N mm/mm for the dynamic and quasi-static analyses, respectively. Thus, the energy dissipated from the dynamic analysis is higher. The results imply that the processes that arise within the sample, once the crack initiates, are dynamic ones. Thus, a dynamic analysis should be adopted to study the fracture process.

5.4 Asymmetric Double-Edge Notched Tensile Sample. A square sample with an asymmetric double notch, subjected to uniaxial tension is tested in this example as shown in Fig. 7(*a*). The top and bottom edges are under uniaxial tension where the applied velocity is 10^{-3} mm/s in the vertical direction, maintaining the horizontal displacement to zero. The sample is discretized by 28,531 quadrilateral elements of an unstructured mesh.

Figures 7(*b*) and (*c*) show the relative density contours under different levels of remote tension. Cracks initiate from both notches and propagate in straight paths. Then, the two propagating cracks branch and continue propagating until each crack reaches the vicinity of the other crack. At this point, the branch of each crack that is far away from the other crack arrests while the branch that is close to the other crack continues propagating and then bridges with its counterpart branch propagating from the other crack.

The same example has been tested in the quasi-static case [65]. The results did not encompass any branching (Fig. 11(*d*)). On the other hand, the result from the dynamic analysis as shown in Fig. 7 shows branching and dynamic crack propagation. It is evident that cracks propagate dynamically and should be analyzed dynamically.

5.5 Three-Dimensional Dog-Bone-Shaped Sample. A 3D dog-bone-shaped sample is modeled, where its geometric setup and boundary conditions are depicted in Fig. 8(*a*) with a thickness of 0.2 mm. The top and bottom surfaces are moving with prescribed

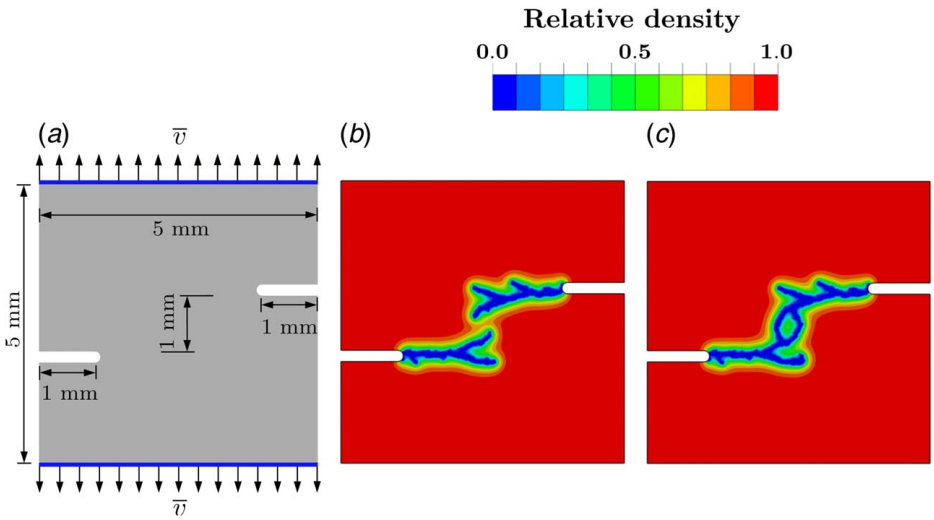

Fig. 7 Asymmetric double-edge notched tensile sample: (*a*) geometry and boundary conditions with an applied velocity $\overline{v}$ equals 10^{-3} mm/s; relative density (i.e., γ) distribution under different levels of remote tension, (*b*) cracks branching and arrest, and (c) bridging between the two cracks

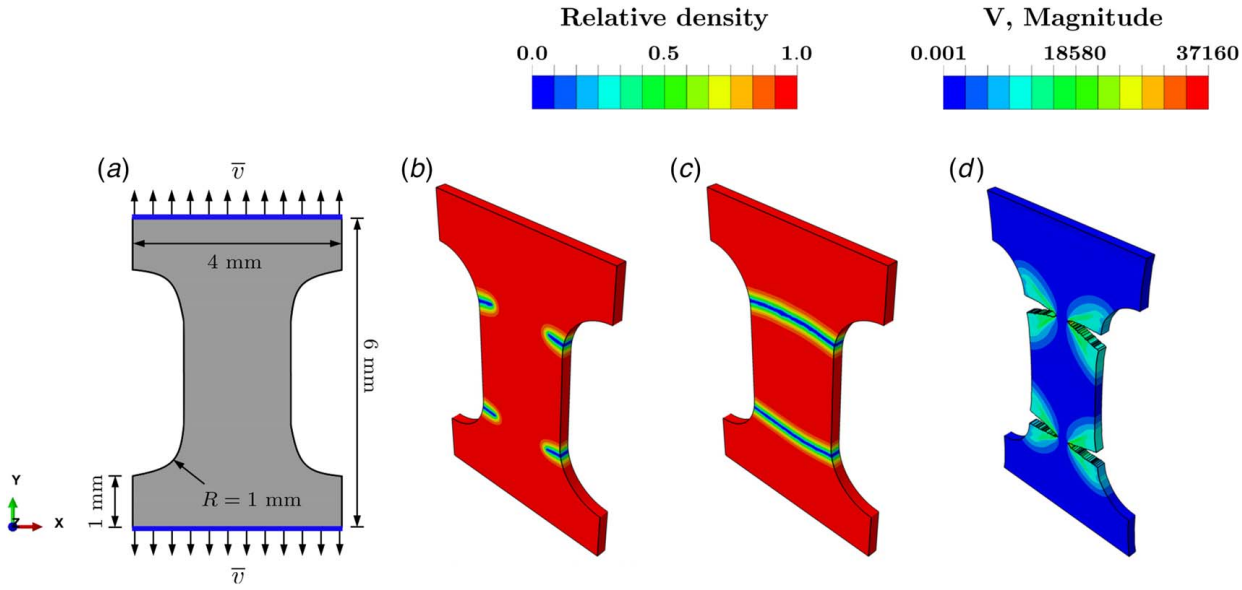

Fig. 8 Dog-bone-shaped sample: (*a*) geometry and boundary conditions with an applied velocity $\overline{v}$ equals 10^{-3} mm/s, (*b*) and (*c*) relative density (i.e., γ) distribution under different levels of remote tension, and (*d*) velocity contours in mm/s on the deformed configuration during crack propagation

velocity having a magnitude of 10^{-3} mm/s in the y-direction. Moreover, the top and bottom surfaces are restricted to move in the x and z directions. The specimen's domain is discretized by 82,382 bricks of unstructured mesh.

Figures 8(*b*) and (*c*) depict the relative density contours at different levels of remote tension. A crack initiates and propagates in a straight line from each intersection point—between the fillet and the narrow section—which merges with the crack that comes from the opposite side. The results do not show any branching in this example, which may be attributed to the lack of enough space required for branching. In other words, although the crack propagates dynamically with a very high velocity (nearly 37 million times the applied velocity) as depicted in Fig. 8(*d*), its path is similar to a quasi-static path (Fig. 11(*e*)) that does not enclose branching. The latter may be due to the lack of enough distance that the propagating crack needs for branching.

The results suggest that there are cases in which the crack propagates dynamically with a path similar to the quasi-static path. The latter may imply that, in these cases, the quasi-static analysis is enough for such modeling. However, it is not always possible to know if a quasi-static analysis will be enough beforehand. Knowing if the distance that the sample provides will be enough or not for branching cannot be known without carrying out a dynamic analysis in advance.

5.6 Cylindrical Shell. A half of a thin-walled cylinder is modeled in this subsection. Its right and left ends are under uniaxial velocity in the axial direction (z-direction) having a magnitude of 10^{-3} mm/s as depicted in Fig. 9. Furthermore, the right and left ends are restricted in the x and y directions. The inner radius r_i is 1.9 mm, while the thickness is 0.1 mm. A pre-existing notch is introduced in the mid-distance of the cylinder. The specimen's domain is discretized by 53,122 elements of unstructured bricks.

Figure 10 shows the relative density contours at different levels of remote tension on the deformed shape. Two cracks initiate from both sides of the pre-existing notch and follow the mode I direction along the curved geometry in straight lines. Then, each crack branches into two branches as depicted in Fig. 10(*a*). These branches reach the end of the sample that is fractured into four pieces, where Fig. 10(*b*) shows the sample's status just when the cracks reach the end of the sample. Figures 10(*c*) and (*d*) depict the specimen's status just after its separation. After the specimen's fracture, waves propagate along the cylinder, and then these waves are broken by the prescribed velocity boundary condition (i.e., reflections at the boundaries), forcing them to propagate back toward the fractured zone.

On the other hand, the crack propagation path in the quasi-static paper [65], for a similar example, was a straight line path perpendicular to the tensile loading following mode I direction along the curved geometry as shown in Fig. 11(*f*). However, it can be noticed from the dynamic analysis in Fig. 10 that although the applied velocity is small (quasi-static), the fracture is a dynamic process that cannot be captured via quasi-static analysis. The latter remark implies that fracture modeling should be carried out using a dynamic analysis that can capture all the processes during the specimen's fracture.

Ultimately, dynamic analysis is important to capture all the dynamic processes occurring once the crack starts initiating. The latter note is highly important since all the processes occurring within the specimen after crack initiation are dynamic ones and should be analyzed via dynamic analysis.

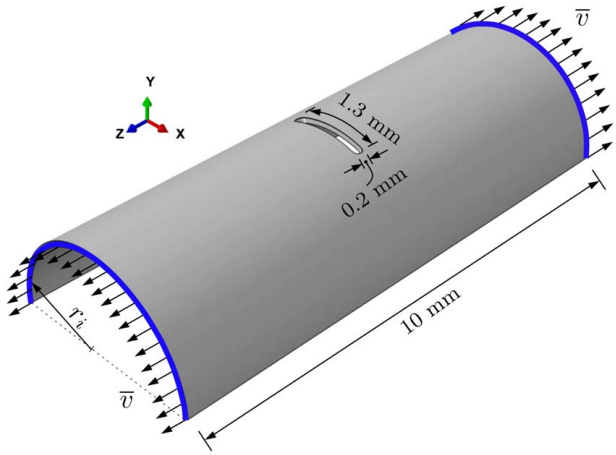

Fig. 9 The geometry of half of the thin-walled cylinder. The applied velocity $\overline{v}$ equals 10^{-3} mm/s.

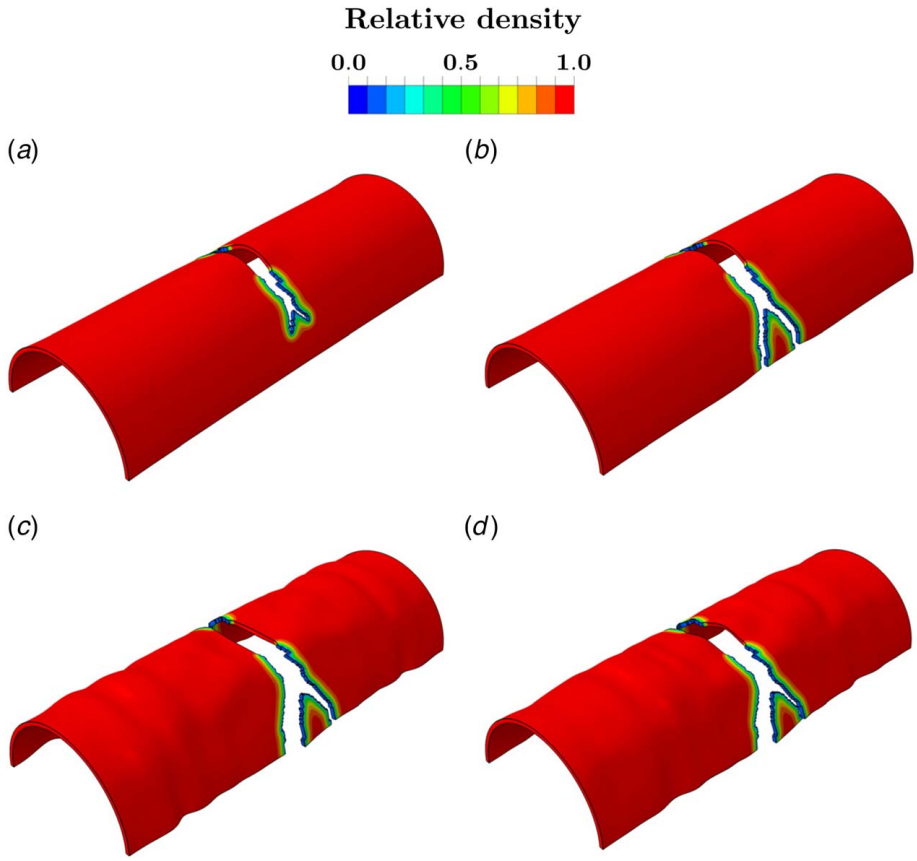

Fig. 10 Half of a thin-walled cylinder sample: relative density (i.e., γ) distribution under different levels of remote tension (*a*) when cracks branch, (*b*) when cracks just reach the end of the sample, and (c) and (*d*) after the specimen's fracture causing wave propagation as a result of the specimen's separation

6 Conclusions

In this work, the MS method was used to model dynamic fracture. It aimed to study whether cracks propagate quasi-statically or dynamically after the onset of material instability and damage. Various examples were analyzed dynamically under the quasi-static (very slow) loads. Results of the dynamic analyses were compared to the quasi-static ones [65].

For a single-edge notched sample under quasi-static tension, we observed that crack propagated fast and branched dynamically. However, no branching was observed in the purely quasi-static simulations.

Similarly, in the cases of both asymmetric and symmetric double-edge notched samples under quasi-static tension, cracks propagated dynamically and branched in contrast to the purely quasi-static simulations.

A simple shear example demonstrated that the crack patterns for the dynamic and quasi-static analyses were similar. However, the dissipated energy in the dynamic analysis was higher.

Dynamic analysis of a three-dimensional dog-bone-shaped sample showed a crack propagating dynamically at high velocity with a path similar to the quasi-static one. The similarity can be attributed to the short length of the propagating cracks. Lengthier cracks would branch dynamically.

A cylindrical shell example showed that the crack patterns from the dynamic and quasi-static analyses were different.

It is concluded that cracks propagate dynamically rather than quasi-statically and, additionally, dynamic and quasi-static crack patterns are, generally, different. Thus, cracks should be analyzed dynamically to capture the fast fracture processes occurring after the onset of material instability and damage localization.

Acknowledgment

The support from Israel Science Foundation (ISF-394/20) is gratefully acknowledged. Also, M. Jabareen is supported by Neubauer Foundation.

Conflict of Interest

The authors declare that they have no known competing financial interests or personal relationships that could have appeared to influence the work reported in this paper.

Data Availability Statement

The datasets generated and supporting the findings of this article are obtainable from the corresponding author upon reasonable request.

Appendix: Results From the Quasi-Static Analysis

The relative density contours from Ref. [65] when the quasi-static analysis was adopted are shown in Fig. 11. It should be emphasized that those results (Fig. 11) are not products of the current work, rather they are products of a previous study conducted by the authors of a quasi-static analysis of crack propagation [65]. They are only presented in this study to compare those results achieved from quasi-static analysis to the results of dynamic analysis acquired from the current study. For more details about the quasi-static analysis, interested readers are advised to consult the former paper [65].

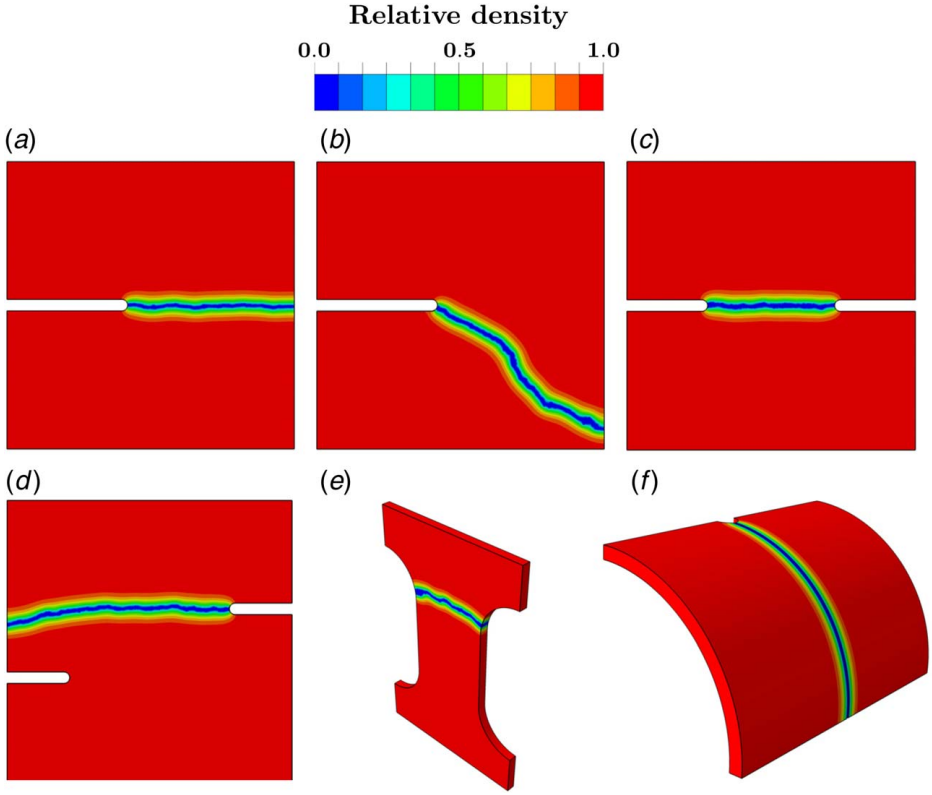

Fig. 11 Relative density (i.e., γ) distribution from the quasi-static analysis [65]: (*a*) single-edge notched tensile sample, (*b*) simple shear test, (*c*) symmetric double-edge notched tensile sample, (*d*) asymmetric double-edge notched tensile sample, (*e*) three-dimensional dog-bone-shaped sample, and (*f*) cylindrical shell

References

[1] Griffith, A. A., 1921, "The Phenomena of Rupture and Flow in Solids," Phil. Trans. R. Soc. Lond. Ser. A, Contain. Pap. Math. Phys. Charact., **221**(582–593), pp. 163–198.

[2] Molnár, G., Gravouil, A., Seghir, R., and Réthoré, J., 2020, "An Open-Source Abaqus Implementation of the Phase-Field Method to Study the Effect of Plasticity on the Instantaneous Fracture Toughness in Dynamic Crack Propagation," Comput. Methods Appl. Mech. Eng., **365**, p. 113004.

[3] Elishakoff, I., and Volokh, K. Y., 2021, "Centenary of Two Pioneering Theories in Mechanics," Math. Mech. Solids, **26**(12), pp. 1896–1904.

[4] Irwin, G. R., 1958, "Fracture," *Elasticity and Plasticity/Elastizität und Plastizität. Handbuch der Physik/Encyclopedia of Physics*, S. Flügge, ed., Springer, Berlin, Heidelberg, pp. 551–590.

[5] Bui, H., 1978, *Mécanique De La Rupture Fragile*, Masson, Paris.

[6] Adda-Bedia, M., Arias, R., Ben Amar, M., and Lund, F., 1999, "Generalized Griffith Criterion for Dynamic Fracture and the Stability of Crack Motion at High Velocities," Phys. Rev. E, **60**(2), pp. 2366–2376.

[7] Freund, L., 1998, *Dynamic Fracture Mechanics*, Cambridge University Press, Cambridge.

[8] Rice, J. R., 2001, *Some Studies of Crack Dynamics*, Springer Netherlands, Dordrecht.

[9] Kanninen, M., and Popelar, C., 1985, *Advanced Fracture Mechanics*, 1st ed., Oxford University Press, New York.

[10] Maigre, H., and Rittel, D., 1993, "Mixed-Mode Quantification for Dynamic Fracture Initiation: Application to the Compact Compression Specimen," Int. J. Solids Struct., **30**(23), pp. 3233–3244.

[11] Zhou, M., Rosakis, A., and Ravichandran, G., 1996, "Dynamically Propagating Shear Bands in Impact-Loaded Prenotched Plates—i. Experimental Investigations of Temperature Signatures and Propagation Speed," J. Mech. Phys. Solids, **44**(6), pp. 981–1006.

[12] Kalthoff, J. F., 2000, "Modes of Dynamic Shear Failure in Solids," Int. J. Fracture, **101**(1), pp. 1–31.

[13] Wunderlich, W., and Awaji, H., 2001, "Molecular Dynamics – Simulations of the Fracture Toughness of Sapphire," Mater. Des., **22**(1), pp. 53–59.

[14] Zhou, S. J., Lomdahl, P. S., Thomson, R., and Holian, B. L., 1996, "Dynamic Crack Processes Via Molecular Dynamics," Phys. Rev. Lett., **76**(13), pp. 2318–2321.

[15] Rountree, C. L., Kalia, R. K., Lidorikis, E., Nakano, A., Van Brutzel, L., and Vashishta, P., 2002, "Atomistic Aspects of Crack Propagation in Brittle Materials: Multimillion Atom Molecular Dynamics Simulations," Annu. Rev. Mater. Res., **32**(1), pp. 377–400.

[16] Barenblatt, G. I., 1959, "The Formation of Equilibrium Cracks During Brittle Fracture. General Ideas and Hypotheses. Axially-Symmetric Cracks," J. Appl. Math. Mech., **23**(3), pp. 622–636.

[17] Needleman, A., 1987, "A Continuum Model for Void Nucleation by Inclusion Debonding," ASME J. Appl. Mech., **54**(3), pp. 525–531.

[18] Rice, J. R., and Wang, J. -S., 1989, "Embrittlement of Interfaces by Solute Segregation," Mater. Sci. Eng. A, **107**, pp. 23–40.

[19] Tvergaard, V., and Hutchinson, J. W., 1992, "The Relation Between Crack Growth Resistance and Fracture Process Parameters in Elastic–Plastic Solids," J. Mech. Phys. Solids., **40**(6), pp. 1377–1397.

[20] Camacho, G. T., and Ortiz, M., 1996, "Computational Modelling of Impact Damage in Brittle Materials," Int. J. Solids Struct., **33**(20), pp. 2899–2938.

[21] Borst, R. d., 2001, "Some Recent Issues in Computational Failure Mechanics," Int. J. Numer. Methods Eng., **52**(1–2), pp. 63–95.

[22] Xu, X. P., and Needleman, A., 1994, "Numerical Simulations of Fast Crack Growth in Brittle Solids," J. Mech. Phys. Solids, **42**(9), pp. 1397–1434.

[23] Moes, N., Dolbow, J., and Belytschko, T., 1999, "A Finite Element Method for Crack Growth Without Remeshing," Int. J. Numer. Methods Eng., **46**(1), pp. 131–150.

[24] Zhou, F., and Molinari, J. F., 2004, "Dynamic Crack Propagation With Cohesive Elements: A Methodology to Address Mesh Dependency," Int. J. Numer. Methods Eng., **59**(1), pp. 1–24.

[25] Azevedo, N. M., and Lemos, J., 2006, "Hybrid Discrete Element/Finite Element Method for Fracture Analysis," Comput. Methods Appl. Mech. Eng., **195**(33), pp. 4579–4593.

[26] Park, K., Paulino, G. H., and Roesler, J. R., 2009, "A Unified Potential-Based Cohesive Model of Mixed-Mode Fracture," J. Mech. Phys. Solids, **57**(6), pp. 891–908.

[27] Peng, G. L., and Wang, Y. H., 2012, "A Node Split Method for Crack Growth Problem," Appl. Mech. Mater., **182–183**, pp. 1524–1528.

[28] Gong, B., Paggi, M., and Carpinteri, A., 2012, "A Cohesive Crack Model Coupled With Damage for Interface Fatigue Problems," Int. J. Fracture, **173**(2), pp. 91–104.

[29] Moes, N., Gravouil, A., and Belytschko, T., 2002, "Non-Planar 3D Crack Growth by the Extended Finite Element and Level Sets—Part I: Mechanical Model," Int. J. Numer. Methods Eng., **53**(11), pp. 2549–2568.

[30] Msekh, M. A., Sargado, J. M., Jamshidian, M., Areias, P. M., and Rabczuk, T., 2015, "Abaqus Implementation of Phase-Field Model for Brittle Fracture," Comput. Mater. Sci., **96**, pp. 472–484.

[31] Bui, T. Q., and Tran, H. T., 2021, "A Localized Mass-Field Damage Model With Energy Decomposition: Formulation and Fe Implementation," Comput. Methods Appl. Mech. Eng., **387**, p. 114134.

[32] Kachanov, L. M., 1958, "Time of the Rupture Process Under Creep Conditions," Izv Akad Nauk SSSR, Otdelenie Teckhnicheskikh Nauk, **8**, pp. 26–31.
[33] Gurson, A. L., 1977, "Continuum Theory of Ductile Rupture by Void Nucleation and Growth: Part I—Yield Criteria and Flow Rules for Porous Ductile Media," ASME J. Eng. Mater. Technol., **99**(1), pp. 2–15.
[34] Voyiadjis, G. Z., and Kattan, P. I., 1992, "A Plasticity-Damage Theory for Large Deformation of Solids–I. Theoretical Formulation," Int. J. Eng. Sci., **30**(9), pp. 1089–1108.
[35] Gao, H., and Klein, P., 1998, "Numerical Simulation of Crack Growth in an Isotropic Solid With Randomized Internal Cohesive Bonds," J. Mech. Phys. Solids, **46**(2), pp. 187–218.
[36] Klein, P., and Gao, H., 1998, "Crack Nucleation and Growth As Strain Localization in a Virtual-Bond Continuum," Eng. Fract. Mech., **61**(1), pp. 21–48.
[37] Lemaitre, J., and Desmorat, R., 2005, *Engineering Damage Mechanics: Ductile, Creep, Fatigue and Brittle Failures*, Springer, Berlin/Heidelberg.
[38] Volokh, K. Y., 2004, "Nonlinear Elasticity for Modeling Fracture of Isotropic Brittle Solids," ASME J. Appl. Mech., **71**(1), pp. 141–143.
[39] Benzerga, A. A., Leblond, J. -B., Needleman, A., and Tvergaard, V., 2016, "Ductile Failure Modeling," Int. J. Fracture, **201**(1), pp. 29–80.
[40] Pijaudier-Cabot, G., and Bažant, Z. P., 1987, "Nonlocal Damage Theory," J. Eng. Mech., **113**(10), pp. 1512–1533.
[41] Lasry, D., and Belytschko, T., 1988, "Localization Limiters in Transient Problems," Int. J. Solids Struct., **24**(6), pp. 581–597.
[42] Peerlings, R. H. J., de Borst, R., Brekelmans, W. A. M., and de Vree, J. H. P., 1996, "Gradient Enhanced Damage for Quasi-Brittle Materials," Int. J. Numer. Methods Eng., **39**(19), pp. 3391–3403.
[43] de Borst, R., and van der Giessen, E., 1998, *Material Instabilities in Solids*, Wiley, Chichester.
[44] Silling, S. A., 2000, "Reformulation of Elasticity Theory for Discontinuities and Long-Range Forces," J. Mech. Phys. Solids, **48**(1), pp. 175–209.
[45] Francfort, G. A., and Marigo, J. J., 1998, "Revisiting Brittle Fracture As an Energy Minimization Problem," J. Mech. Phys. Solids, **46**(8), pp. 1319–1342.
[46] Bourdin, B., Francfort, G. A., and Marigo, J.-J., 2000, "Numerical Experiments in Revisited Brittle Fracture," J. Mech. Phys. Solids., **48**(4), pp. 797–826.
[47] Miehe, C., Hofacker, M., and Welschinger, F., 2010, "A Phase Field Model for Rate-Independent Crack Propagation: Robust Algorithmic Implementation Based on Operator Splits," Comput. Methods Appl. Mech. Eng., **199**(45), pp. 2765–2778.
[48] Miehe, C., Welschinger, F., and Hofacker, M., 2010, "Thermodynamically Consistent Phase-Field Models of Fracture: Variational Principles and Multi-field Fe Implementations," Int. J. Numer. Methods Eng., **83**(10), pp. 1273–1311.
[49] Hofacker, M., and Miehe, C., 2012, "A Phase Field Model of Dynamic Fracture: Robust Field Updates for the Analysis of Complex Crack Patterns," Int. J. Numer. Methods Eng., **93**(3), pp. 276–301.
[50] Hofacker, M., and Miehe, C., 2012, "Continuum Phase Field Modeling of Dynamic Fracture: Variational Principles and Staggered Fe Implementation," Int. J. Fracture, **178**(1), pp. 113–129.
[51] Borden, M. J., Verhoosel, C. V., Scott, M. A., Hughes, T. J. R., and Landis, C. M., 2012, "A Phase-Field Description of Dynamic Brittle Fracture," Comput. Methods Appl. Mech. Eng., **217–220**, pp. 77–95.
[52] Liu, G., Li, Q., Msekh, M. A., and Zuo, Z., 2016, "Abaqus Implementation of Monolithic and Staggered Schemes for Quasi-Static and Dynamic Fracture Phase-Field Model," Comput. Mater. Sci., **121**, pp. 35–47.
[53] Miehe, C., and Schänzel, L.-M., 2014, "Phase Field Modeling of Fracture in Rubbery Polymers. Part I: Finite Elasticity Coupled With Brittle Failure," J. Mech. Phys. Solids, **65**, pp. 93–113.
[54] Raina, A., and Miehe, C., 2016, "A Phase-Field Model for Fracture in Biological Tissues," Biomech. Model. Mechanobiol., **15**(3), pp. 479–496.
[55] Miehe, C., Aldakheel, F., and Raina, A., 2016, "Phase Field Modeling of Ductile Fracture at Finite Strains: A Variational Gradient-Extended Plasticity-Damage Theory," Int. J. Plast., **84**, pp. 1–32.
[56] Wu, J.-Y., and Huang, Y., 2020, "Comprehensive Implementations of Phase-Field Damage Models in Abaqus," Theor. Appl. Fract. Mech., **106**, p. 102440.
[57] Russ, J., Slesarenko, V., Rudykh, S., and Waisman, H., 2020, "Rupture of 3D-Printed Hyperelastic Composites: Experiments and Phase Field Fracture Modeling," J. Mech. Phys. Solids, **140**, p. 103941.
[58] Volokh, K. Y., 2017, "Fracture As a Material Sink," Mater. Theory, **1**(1), p. 3.
[59] Volokh, K. Y., 2007, "Hyperelasticity With Softening for Modeling Materials Failure," J. Mech. Phys. Solids, **55**(10), pp. 2237–2264.
[60] Volokh, K. Y., 2010, "On Modeling Failure of Rubber-Like Materials," Mech. Res. Commun., **37**(8), pp. 684–689.
[61] Volokh, K. Y., 2011, "Characteristic Length of Damage Localization in Rubber," Int. J. Fracture, **168**(1), pp. 113–116.
[62] Volokh, K. Y., 2013, "Review of the Energy Limiters Approach to Modeling Failure of Rubber," Rubber Chem. Technol., **86**(3), pp. 470–487.
[63] Volokh, K. Y., 2013, "Characteristic Length of Damage Localization in Concrete," Mech. Res. Commun., **51**, pp. 29–31.
[64] Volokh, K. Y., 2019, *Mechanics of Soft Materials*, 2nd ed., Springer, Singapore.
[65] Abu-Qbeitah, S., Jabareen, M., and Volokh, K., 2022, "Quasi-Static Crack Propagation in Soft Materials Using the Material-Sink Theory," submitted.
[66] Lorentz, E., and Benallal, A., 2005, "Gradient Constitutive Relations: Numerical Aspects and Application to Gradient Damage," Comput. Methods Appl. Mech. Eng., **194**(50), pp. 5191–5220.
[67] Chaboche, J. L., Feyel, F., and Monerie, Y., 2001, "Interface Debonding Models: A Viscous Regularization With a Limited Rate Dependency," Int. J. Solids Struct., **38**(18), pp. 3127–3160.
[68] Wick, T., 2017, "Modified Newton Methods for Solving Fully Monolithic Phase-Field Quasi-Static Brittle Fracture Propagation," Comput. Methods Appl. Mech. Eng., **325**, pp. 577–611.
[69] Bishara, D., and Jabareen, M., 2018, "A Reduced Mixed Finite-Element Formulation for Modeling the Viscoelastic Response of Electro-Active Polymers at Finite Deformation," Math. Mech. Solids, **24**(5), pp. 1578–1610.
[70] Jabareen, M., 2020, "A Polygonal Finite Element Formulation for Modeling Nearly Incompressible Materials," Meccanica, **55**(4), pp. 701–723.
[71] Hilber, H., Hughes, T., and Taylor, R., 1977, "Improved Numerical Dissipation for Time Integration Algorithms in Structural Dynamics," Earthquake Eng. Struct. Dyn., **5**(3), pp. 283–292.
[72] Smith, M., 2020, *ABAQUS/Standard Documentation*, Version 2020, Johnston, RI.
[73] Roth, S., Hütter, G., Mühlich, U., Nassauer, B., Zybell, L., and Kuna, M., 2012, "Visualisation of User Defined Finite Elements With Abaqus/Viewer," Institute of Mechanics and Fluid Dynamics, TU Bergakademie Freiberg.
[74] Faye, A., Lev, Y., and Volokh, K. Y., 2019, "The Effect of Local Inertia Around the Crack-Tip in Dynamic Fracture of Soft Materials," Mech. Soft Mater., **1**(1), pp. 4.
[75] Raghavan, M. L., and Vorp, D. A., 2000, "Toward a Biomechanical Tool to Evaluate Rupture Potential of Abdominal Aortic Aneurysm: Identification of a Finite Strain Constitutive Model and Evaluation of Its Applicability," J. Biomech., **33**(4), pp. 475–482.
[76] Gerasimov, T., and Lorenzis, L. D., 2016, "A Line Search Assisted Monolithic Approach for Phase-Field Computing of Brittle Fracture," Comput. Methods Appl. Mech. Eng., **312**, pp. 276–303.